Novel algorithm for retrieving spatial scale of precipitating clouds from low-orbiting satellite observations

LIU Qi, FU Yunfei, WANG Yu

Laboratory of Atmospheric Observation and Climatological Environment, School of Earth and Space Sciences, University of Science and Technology of China, Anhui Hefei 230026, *China*

Abstract: A new scheme was proposed in this study to account for such a handicap, which is based on the statistics of object area fraction that is somewhat insensitive to the orbit truncation. In order to get a measurement that could be accurately received, continuous circle object was consulted. Accordingly the equivalent radius was finally defined by using a minimum deviation principle to indicate the object scale. Since the equivalent radius is an indirect indicator of object spatial scale, it could be used as a secondary strategy to modify the results from counting method, by which the underestimate would be restrained to some extent.

Key words: precipitating clouds, spatial scale, object area fraction, equivalent radius

CLC number: TP79 **Document code:** A

Citation format: Liu Q, Fu Y F and Wang Y. 2010. Novel algorithm for retrieving spatial scale of precipitating clouds from low-orbiting satellite observations. *Journal of Remote Sensing.* **14**(4): 774—788

1 INTRODUCTION

The size variation of cloud associated with its formation and decline is closely correlative with large-scale circulation situation, for which it is very indicative for the weather in near future (Wang & Liu, 2007). With similar function as those common cloud macro- and microphysics such as cloud life-time, cloud water path, cloud optical thickness and cloud-drop effective radius, the spatial scale of clouds is also important reference for estimating surface rainfall (Rosenfeld & Gagin, 1989).

Since geostationary orbit satellites supply continuous observations on a large scale, they have been used as a primary means in global precipitation surveillance for several decades (Arkin, 1979; Arkin & Meisner, 1987; King, 1987). Benefiting from the acquired visible/infrared image about clouds and underlying surface, the spatial distribution of specific type of clouds can be portrayed with considerable accuracy (Machado *et al.*, 1992; Rossow, 1989). However, the observation of geostationary orbit satellites is incapable for precipitation as well as precipitating clouds. Within visible and infrared spectrum, the radiation is highly attenuated by cloud droplets both through scattering and absorption processes, resulting in that there is little information about precipitation in the satellite-derived signals (Olson *et al*., 1996). Due to the inability of visible and infrared techniques in detecting instantaneous precipitation, such observations cannot be used to deduce precipitating cloud parameters (Smith, 2005). Microwave remote sensing is the only available way in satellite-based precipitation observation, which relies on the deep penetration into lower precipitation layers of microwave radiation. Because of technical limitations, microwave sensors including active radar and passive radiometer, so far can only be loaded on low-orbiting satellite to obtain satisfactory horizontal resolution, which is restricted by wavelength employed and satellite orbit altitude. For instance, measurements from SSMI (Special Sensor Microwave Imager) aboard DMSP (Defense Meteorological Satellite Program) satellite along with TRMM Microwave Imager (TMI) aboard TRMM (Tropical Rainfall Measuring Mission) satellite were commonly used to clarify the structure of precipitation system, revealing that the horizontal scale of most precipitating clouds is less than 100km (Genio & Kovari, 2002; Mohr & Zipser, 1996; Nesbitt *et al*., 2000).

Clouds are inherently scattered with irregular spatial structures, making it difficult to get an accurate estimation of the cloudy area. In satellite remote sensing, detecting and counting continuous cloudy pixels is an alternative. Thus the cloud area can be characterized by the equivalent-area circle radius. Such a method is well applicable to the semi-disk observations from geostationary orbit satellite, but it encounters handicap when applied to cross-scanning measurements from low-orbiting satellite because of their rather limited swath width (e.g., the two microwave sensors aboard TRMM satellite platform, TMI 760km, Precipitation Radar 220km). This means only a few clouds or precipitation can be completely covered by the individual swath, whereas lots of them are not fully sampled by satellite observations. As shown in Fig.1, incomplete detection and corresponding biased pixel-counting inevitably lead to underestimation of precipitation area.

Received: 2009-07-03; **Accepted**: 2010-03-22

Foundation: National Natural Science Foundation of China (No. 40805007), Postdoctoral Science Foundation of China (No. 20080430099 and No. 200801232).

First author biography: LIU Qi (1980—), male, Associate Professor, E-mail: lqee@ustc.edu

Corresponding author: FU Yunfei, E-mail: fyf@ustc.edu.cn

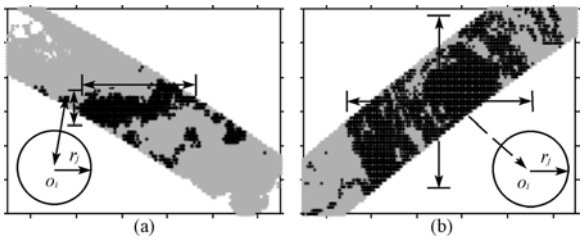

Fig. 1 Schematic diagram for the horizontal scale of precipitating clouds
(a) In frontal domain; (b) Typhoon domain
Black and grey pixels indicate precipitating and non-precipitating clouds, respectively, while the rest white pixels within swath indicate clear-sky area. The O_i represents the i-th reference centre, which covers all precipitating clouds in this case. The r_j represents j-th reference radius

Nesbitt *et al.* (2000) carried statistics on TRMM PR measurements, and concluded that there are 17% tropical precipitation systems and 82% mesoscale convective systems affected by such situation of incomplete coverage of swath, called swath-truncation effect. Hence, the area results would get largely biased when the characteristic scale of concerned object is larger than the orbit swath width. It is easy to confer that larger objects get more serious underestimation if pixel-counting method was employed. In particular, the biases in precipitation area estimation would be propagated into the phase of surface rainfall deduction, which gets more uncertain and thus unreliable.

As shown in Fig.1, actual precipitating clouds tend to scatter and appear various shapes when compared with non-precipitating clouds that act as cloudy background. Although image-based measuring method can intuitively characterize the object size with the range of length and width, its estimation is less quantitative because of its inability for excluding scattered non-object. In addition, such a method is only available for case-analysis under continuous surveillances (Fu *et al.*, 2005), but not for automatic procedures that process massive satellite measurements. This study proposes a new method to retrieve the horizontal scale of precipitating clouds from low-orbiting satellite measurements with lower uncertainty, which can mitigate swath-truncation effect to some extent.

2 EQUIVALNT RADIUS METHOD

For generality, herein we do not refer to concrete matters such as cloud or precipitation, but consider any target requiring scale decision as an acceptable object. Such an object is macro matter that generally consists of multiple meta-components that could be termed as object points for simplicity. A reasonable presumption is that each observed point (pixel for satellite remote sensing) has been accurately identified and classified as an object or non-object point. The issue to be solved by the present algorithm is to give an estimation of object scale with less impact from swath-truncation effect, by using information of the acquired distribution of object and non-object points within the limited swath. Since no other specific information is needed, besides above precipitating clouds we consider, this method can be used also to low-orbiting applications like remote sensing of precipitation (McCollum & Ferraro, 2003; Fu & Liu, 2003; Shige *et al.*, 2006), aerosols (Spinhirne *et al.*, 2005; Liu *et al.*, 2008) and fire spots (Fraser *et al.*, 2000).

The pixel-counting method is based on an absolute magnitude determined jointly by the object itself and the swath coverage situation, for which the result is highly biased. It is apparent that the estimated scale would be only half the reality if 50% pixels are covered by a swath. Due to the random of the coverage situation, it is unpractical to add a reliable modification (e.g. some scale and offset index) to the result. On the other hand, the image-based method uses only information about the range at arbitrary orthogonal dimensions but ignore scattering pattern of object/non-object points in the range, which generally results in overestimation of the object scale.

As a deduction, a factor derived from the distribution pattern, which is less sensitive to the swath coverage but accounts for the actual scattering of object/non-object points, is critical to an ideal method. The average of distances between each two object points in a specified domain seems to be a good measure due to its equal-weighted sampling. But it is inherently an absolute magnitude that is also highly affected by swath coverage proportion, and thus is not the ideal method desired.

2.1 Principle of object area fraction

Accounting for issues mentioned above, we propose a method based on object area fraction (OAF). The OAF means the ratio of object points to all observing-valid points in a specified domain. In general, satellite executes observation in the same way for each pixel, resulting in identical resolution and therefore identical area. Hence the number ratio defined is in fact an area ratio, which is related to the location and size of specified domain. As the object considered always has a limited area, the OAF would approach unity if the size is near zero and the center of domain is at an object point, while it would decrease with increasing size because more non-object points gradually enter the domain.

For a designated centre of domain, OAF is a single-variable function of the size of reference domain, with its varying form representative for the scale of object. The most important advantage is that OAF is a relative magnitude without any unit. The OAF can remain almost constant when the borderline of reference domain approaches swath edge, because both object and non-object points decrease dramatically therein. Therefore such an index does not indicate pseudo boundary for the actual object when confronted by swath-truncation. This is the underline base for which it is used for characterizing the horizontal scale of the object.

It is obvious that a circle is the most convenient manner to specify a domain in which OAF can be calculated. Correspondingly the reference domain center and size is determined by the center of circle and radius of circle, respectively, which hereafter we call as reference centre and reference radius. Aforementioned OAF is actually with respect to a given center

and varies with altered reference radius. But a more meaning one should consider all OAFs with respective to all possible reference centre. So average is employed to derive a mean OAF that is representative for the entire object and highly related to the scale of this object. For convenience, the OAF with respect to a single reference centre is called SAF while the averaged one is called MAF hereafter.

The kernel concept of OAF is similar to the CSL proposed by Masunaga *et al.* (2005). But a difficulty in that method is to search a position where the MAF curve dramatically declines, which does not exist in lots of cases due to the complexity of actual object shape. Hence, the derived position is highly uncertain for these cases and the acquired result according to their method is a bit suspicious. The method herein we proposed is also based on MAF but we take advantage of the comparison with circle. If the MAF curve of an actual object is maximally similar to a known circle, the circle radius is called equivalent radius. Such equivalence is with respect to MAF, totally different with area-equivalent radius that is commonly used.

2.2 SAF of ideal circle surface

As defined previously, f is refereed to as the ratio of object point number (area) to the total number (area) of observing-valid points. The mathematic definition is as Eq.(1), where r indicates the reference radius and $S(r)$ indicates the summed area of object points.

$$f(r)=\frac{S(r)}{\pi r^2} \tag{1}$$

Assuming the object is a continuous circle surface with radius R and center located at O, as shown by shaded circle region in Fig.2. The reference center itself should be an object point (this will be explained later). The l is a distance between O and O'. According to three situations demonstrated by (a), (b) and (c) in Fig. 2, $f(l,r)$ is calculated through following three paths.

The simplified deduction for the SAF calculation is given below.

(1) The reference circle is completely encompassed by the object circle as shown in Fig.2(a). Since all points in the reference circle belong to the object, the SAF has a constant value of 1.

$$f_1(l,r)=1,(l\leqslant R, r\leqslant R-l) \tag{2}$$

(2) The reference circle intersects with the object circle as shown in Fig.2(b). In this case, a part of object points are included by the reference circle, complying the condition $R-l\leqslant r \leqslant R+l$. Let $S(l,r)$ represent the area of overlapped surface, which can be expressed as following.

$$\begin{aligned} S_2(l,r)=&r^2\cos^{-1}\left(\frac{r^2+l^2-R^2}{2rl}\right)+\\ &R^2\cos^{-1}\left(\frac{l^2+R^2-r^2}{2lR}\right)-\\ &lR\sqrt{1-\left(\frac{l^2+R^2-r^2}{2lR}\right)^2} \end{aligned} \tag{3}$$

Correspondingly the SAF is formularized as Eq.(4).

$$\begin{aligned} f_2(l,r)=&S(l,r)/\pi r^2\\ =&\frac{1}{\pi}\cos^{-1}\left(\frac{r^2+l^2-R^2}{2rl}\right)+\\ &\frac{R^2}{\pi r^2}\cos^{-1}\left(\frac{l^2+R^2-r^2}{2lR}\right)-\\ &\frac{lR}{\pi r^2}\sqrt{1-\left(\frac{l^2+R^2-r^2}{2lR}\right)^2} \end{aligned} \tag{4}$$

(3) The reference circle completely encompasses the object circle as shown in Fig.2(c). In this case the required condition is $r\geqslant R+l$. Because the object area is finite and constant, the SAF would decrease proportional to increasing squared reference radius.

$$f_3(l,r)=\frac{\pi R^2}{\pi r^2}=\frac{R^2}{r^2} \tag{5}$$

Thus we can calculate accurately SAF given any condition or constraint. Since the formula of SAF is related to the range of reference radius, it is in fact a combined function. For a constant l_0, $f(l_0,r)$ varies among f_1, f_2 and f_3.

According to the above formulas, Fig.3 demonstrates three special cases of SAF calculation. The three curves represent the SAF with reference centre located at object center, a half radius and a radius apart from circle center, respectively, referred to as $f(0)$, $f(R/2)$, $f(R)$. Apparently the curve of $f(R/2)$ represents the general SAF for a circle object. As shown in Fig.3, $f(R/2)$ is continuous throughout the valid range of reference radius. At $0.5R$ and $1.5R$ there are two gaps where the SAF value is 1.0 and 0.444, respectively. When the reference radius is less than $0.5R$, the SAF value is constantly 1.0. When the reference radius is greater than $1.5R$, SAF varies inversely proportional to squared reference radius. In addition, all three curves converge at $2R$ with the SAF values all equal to 0.25.

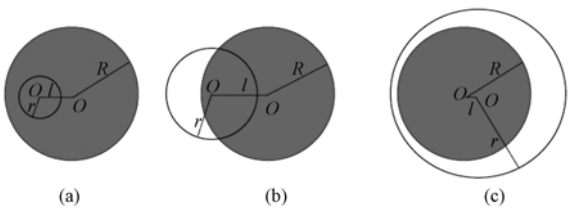

Fig. 2 Schematic diagram for three situations due to distinct spatial correlations between the object circle and the reference circle

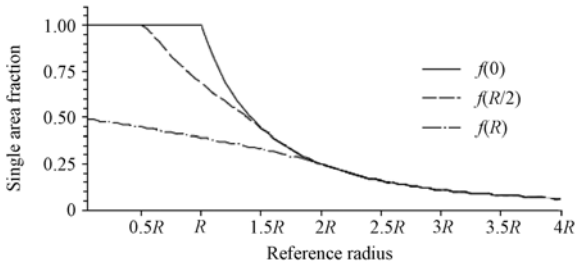

Fig. 3 SAF of three typical situations, with the reference centre located at the object circle center, a half radius apart from center and a radius apart from center, respectively

It is noteworthy that the reference centre can only be designated at any object point (each point inside the shaded circle). This is because that such a restriction can assure the SAF varies from 1.0 as reference radius increases from 0 (It could be proved mathematic-strictly that the SAF starts from 0.5 if the point is at the borderline of object). Thus the averaged MAF is meaningful, with rapid decline of MAF possibly indicating object boundary. A mixture of SAF with respect to object point and SAF with respect to non-object is hard to be interpreted. Additionally, the number of non-object points is generally large while concerned object points are rather limited in reality. Thus the point that should be involved into the SAF calculation is hard to specify if each non-object point can also act as a reference centre. In particular, only designating object as reference centre is beneficial for quickly retrieving the scale of small object.

2.3 MAF of ideal circle surface

As aforementioned, the meaningful curve for characterizing the spatial scale should equally sampling all object points. In practice, we cannot find a unique object point that has more weight than any other. Hence the MAF is calculated by averaging all SAF that uses each object point as reference centre, which is representative for the scale information of entire object. The arithmetic average is performed with respect to all reference centres, resulting in a MAF that is only determined by reference radius. The *F(r)* in following formulas is referred to as MAF. For an object consisting of discrete points, the MAF is expressed as below.

$$F(r_j)=\frac{1}{n}\sum_{i=1}^{n} f(O_i,r_j) \tag{6}$$

While for a circle object on a continuous surface, the expression is an integral as Eq.(7).

$$\begin{aligned} F(r)&=\frac{1}{S}\int_{S_R} f(l,r)\mathrm{d}S \\ &=\frac{1}{\pi R^2}\int_0^R f(l,r)\cdot 2\pi l\mathrm{d}l \end{aligned} \tag{7}$$

Given the three situations in Fig.2, the integral item (f_1 or f_2 or f_3) in above formula is dominated by the value of l. For simplicity, in terms of r, *F(r)* can be calculated via following formulas.

(1) $r\leqslant R$:

$$\begin{aligned} F(r)&=\frac{1}{\pi R^2}\left[\int_0^{R-r} f_1(l,r)\times 2\pi l\mathrm{d}l+\int_{R-r}^{R} f_2(l,r)\times 2\pi l\mathrm{d}l\right] \\ &=\frac{(R-r)^2}{R^2}+\frac{2}{R^2}\int_{R-r}^{R} f_2(l,r)\times l\mathrm{d}l \end{aligned} \tag{8}$$

(2) $R<r\leqslant 2R$:

$$\begin{aligned} F(r)&=\frac{1}{\pi R^2}\left[\int_0^{r-R} f_3(l,r)\times 2\pi l\mathrm{d}l+\int_{r-R}^{R} f_2(l,r)\times 2\pi l\mathrm{d}l\right] \\ &=\frac{(r-R)^2}{r^2}+\frac{2}{R^2}\int_{r-R}^{R} f_2(l,r)\times l\mathrm{d}l \end{aligned} \tag{9}$$

(3) $r>2R$:

$$F(r)=\frac{1}{\pi R^2}\int_0^R f_3(l,r)\times 2\pi l\mathrm{d}l=\frac{R^2}{r^2} \tag{10}$$

Because it is hard to get the analytic result of integral $f_2(l,r)$, we employ numerical scheme to perform the integral throughout the valid range of r. Fig.4 shows the numerically integral result for a continuous circle surface with radius R. The MAF monotonously decreases from 1.0 to near 0.1 at $4R$. It is clear that the value of MAF remains rapid decline between 0 and $2R$. Meanwhile the degression rate reduces constantly without an abrupt variation at any position along the r dimension. This also proves the difficulty for determine a sharply decrease on the MAF curve to estimate CSL as suggested by Masunaga *et al.* (2005). We argue that it is more reasonable to take advantage of information from the entire curve of MAF rather than a particular location.

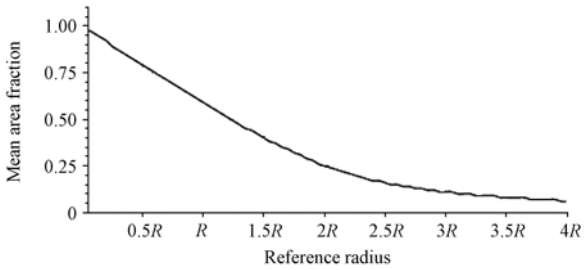

Fig. 4 MAF of ideal circle object that is calculated through numerical integral

2.4 Derivation of equivalent radius

As a deduction from the above graph analysis, herein we determine the equivalent radius based on the principle that the MAF curve of an arbitrary object is maximally similar to the MAF of an ideal circle. In this way, the radius of circle compared was a measure to characterize the scale of considered object, which is thus an equivalent-OAF radius.

By using appropriate scheme, we can obtain $F(d_i),(i=1,M)$ for practical object that consists of discrete points or pixels. Herein d_i equals the r in above formula derivation but with a length unit. The M indicates sampling amount of discrete reference radii. A practical MAF curve, with its left end fixed, can be transformed by stretching/shrinking to most like a given circle MAF curve. If there is a maximum similarity, correspondingly a minimum variance between two series of $F(d_j),(j=1,K)$ and $F(r),(r=0.4R)$, the d_K equals $4R$. Thus the $d_K/4$ is defined herein as equivalent radius and is the desired measure to characterize the scale of an arbitrary object.

Noting that we choose the range of 0 to $4R$ of a circle's MAF as the criterion. Because there are distinct expressions of curve before and after $2R$, this section of curve actually contains sufficient information if the MAF curve and is appropriate for comparison. Due to the necessary of identical sampling amount for calculating variance between two value series, we divide $F(r),(r=0,4R)$ into K parts. Moreover, the sampling for d_i

and correspondingly for r are with constant steps. So the known circle MAF can be further formularized as following equations.

$$\begin{cases} F(r_i), i = 1, K \\ r_i = i \times \Delta r = \dfrac{i \times 4R}{K} \end{cases} \tag{11}$$

Therefore performing stretching/shrinking transformation for derived MAF of an actual object to obtain K is the kernel step of this proposed algorithm. It is obvious that the basic transformation is to directly choose sequent K original sampling points from left end. In order to avoid averaging between original MAF values, the transformation ratio q is designated to be positive integer (1, 2, 3, etc.). The q has a upper limit of $\mathrm{int}(\dfrac{M}{K})$. So for actual MAF, the known conditions are as following.

$$\begin{cases} F(d_i), i = q, qK, q \\ d_i = i \times q \times \Delta d \end{cases} \tag{12}$$

In this way the q_0 is desired, which satisfies conditions below.

$$D(\Delta d, q, K)\,|_{q=q_0} \to \min\{D(\Delta d, q, K)\} \tag{13}$$

Once q_0 is acquired, equivalent-OAF radius is derived by Eq.(14).

$$R_0 = \frac{d_{Kq_0}}{4} = \frac{Kq_0 \times \Delta d}{4} \tag{14}$$

The above mathematic deductions are somewhat expatiatory, but the essence is explicit we believe. Given the curve composed by M points (the interval on r dimension is Δd), we need to choose K ($K \ll M$) points constituting the new curve (the interval on r dimension is $\Delta d'$) under the restriction that $\Delta d'$ equals Δd multiplied by an integer. The K is finally determined if it assure the new curve is maximally similar to the MAF of a circle with radius R. Then the right end of new curve corresponds to $4R$. Due to the upper limit of q, there is below restriction.

$$R_0 = \frac{Kq_0 \times \Delta d}{4} \leqslant \frac{M \times \Delta d}{4} = \frac{L}{4} \tag{15}$$

The L can be deemed as a measure of the maximum domain for statistics. Eq.(15) indicates that L must be large enough. For a too small L, the sampling is possibly insufficient resulting in conditional maximum-similarity. Consequently the derived scale result is uncertain. Furthermore, because q is a positive integer and the Δq (the precision of q_0) is 1, the precision of R_0 can be expressed as Eq.(16).

$$\Delta R = \frac{K \times \Delta q \times \Delta d}{4} = \frac{K \times \Delta d}{4} \tag{16}$$

Besides the Δd, the precision of R_0 is also related to K. So the value of K cannot be specified to be too large. On the other hand, a too small K would lead to inaccurate characterization of a curve. Hence, K should be moderate and appropriate to practical cases. For later examples tested that is extracted from TRMM PR observations, we designate Δd as being 5km that is near the PR horizontal resolution and K as being 20. As a consequence, the calculated precision of R_0 is 25km.

3 APPLICATION EXAMPLES

We have tested this algorithm by using TRMM PR precipitation measurements. The dataset in East Asia during 2005 summer was specifically chosen, considering more precipitation events therein. Due to a re-boost of TRMM satellite in August 2001, the PR horizontal resolution is now about 4.9km with a swath width near 250km. Since there are two distinct categories of precipitation typical for summer precipitation in East Asia and their morphologies are largely different, the chose samples that involve dense precipitating clouds were divided into two categories. Among these total 23 samples, the number of frontal and typhoon precipitation is 12 and 11, respectively. We calculated the equivalent-OAF radius for individual samples, and then estimated the averaged scale for each category.

The statistical domain is designated to be an orbit segment within 10^o range along longitude that can almost contain all dense precipitating clouds in a precipitation system, satisfying the criterion of L as suggested by the above discussion. The total amount of ergodic pixels in such a domain is less than 16000. The interval of sampling reference radius is 5km and the maximum sampling distance is 2000km. Fig.5(a) and Fig.5(c) show the MAF calculations for each sample in two categories. It is clearly demonstrated that the practical MAF depart from ideal circle MAF to a large extent. It seems that the difference among the MAF of individual frontal precipitating clouds is more evident than that of typhoon ones. This is possibly caused by generally similar pattern of typhoon systems that are near circle. Although the spatial distribution of frontal system is near a belt almost across west to east, there are significant differences among the detailed structures of precipitating clouds in these precipitation systems.

It is shown by Fig.5(b) and Fig.5(d) that actual MAF curves are more flat than that of ideal circle MAF, suggesting less variability of MAF with increase reference radius. We presume this pattern of actual MAF is related to discontinuous distribution of precipitating cloudy pixels. In fact, there is not a clear boundary surrounding the precipitating clouds and scattering is quite common especially the precipitation center. Moreover, it is noteworthy that two minimum-variance MAF curves in Fig.5(b) are still totally different with the comparison counterpart. An explanation is that strong scattering precipitating cloudy pixels lead to less comparability of them to a continuous circle surface. These two results of horizontal scale estimation are thus more questionable than the others. The averaged result for the two categories of samples is 283±163km and 297±126km for frontal and typhoon system, respectively. It is proven that the characteristic horizontal scales of precipitating clouds in these two mesoscale weather systems are close. The horizontal scale of precipitating clouds in typhoon is slightly larger than frontal ones, while the higher standard variance of frontal precipitating clouds implies their more various spatial patterns than those in typhoon systems.

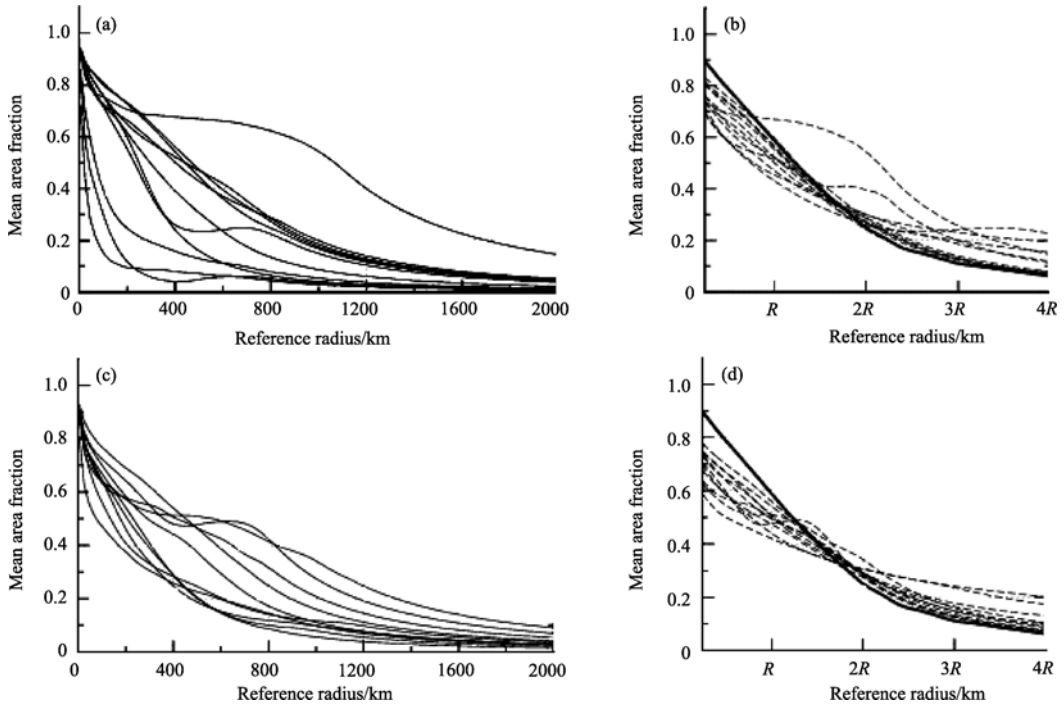

Fig. 5 The individual MAF for frontal (a) and typhoon (c) samples, (b) and (d) are correspondingly the derived minimum-variance curve of MAF, with the solid line indicating MAF of an ideal circle

As a validation, the equivalent-OAF radius derived from current algorithm is compared with the traditionally used equivalent-area radius deduced by a pixel-counting method. The averaged results of equivalent-area radius are 172±52km and 181±25km. Both the close average and larger standard variance of frontal samples suggest similarity with our results despite the evident magnitude difference. Individual comparisons are shown in Fig.6(a) and Fig.6(b). It is apparently demonstrated that our scale results as large as two times to traditional ones for those with equivalent-area radius greater than 150km. Taking into account the 250km of PR swath width, such a comparison reveals that traditional method probably give an underestimate due to swath truncation when its derived diameter value approaches swath width. More significant underestimate emerges for large equivalent-area radius.

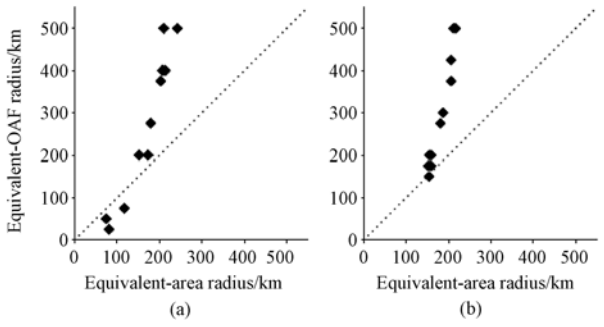

Fig. 6 Comparison between equivalent-OAF radius and traditional equivalent-area radius derived for precipitating clouds in frontal (a) and typhoon (b) systems

4 DISSCUSSIONS

The equivalent-area radius derived from pixel-counting method was commonly used to characterize the horizontal scale of a considered object, since the structures of practical objects are various. Such a method is convenient due to its uniformity on comparative magnitudes. However it has inherent limitation when applied to swath measurements provided by low-orbiting satellites, which suffer from serious swath-truncation effects leading to underestimate of object scale. As a deduction of our analysis, it was deemed that this underestimate is primarily caused by the used area which is an absolute magnitude, greatly affected by the situation of swath coverage. In order to mitigate above effects and achieve a sufficient application of swath measurements of low-orbiting satellite, this study proposed a novel algorithm that employ object area fraction as kernel index to depict the horizontal scale of an arbitrary object. Since such an index is less sensitive to the swath coverage condition, the derived radius based on minimum variance determination is deemed to be more reliable for estimating object scale than traditional results. In fact, object area fraction is similar to area, which is also a feature of the object structure. Although the equivalent-area radius is intuitional, equivalent-OAF radius is more comprehensive in characterizing the object spatial structure.

It is noteworthy that such an equivalent-OAF radius is not a direct measure of the horizontal scale of an arbitrary object. So it is inappropriate to use this radius result to directly estimate the area of considered object. Due to the complexity and diver-

sity of swath truncation conditions, we still need ample statistics as validation to relate such an estimate in terms of radius with the actual object area. Considering the close relationship between area-equivalent derived radius and object area, we suppose a combination of these two indices maybe more efficient for characterizing object area. A reasonable method may first estimate the scale by using equivalent-area radius and then modify the result by using object area fraction calculations.

As for the proposed equivalent-OAF scheme, this study only provides complete mathematic principles. The implied inhibiting function on swath-truncation effects of such a method is not well proved. It is obvious the detailed morphology of objects will inevitably affect our results. More validations are necessary which take advantage of numerical calculations on random situations of swath-truncation. Meanwhile, it is notable that such a method can mitigate to some extent the swath-truncation effects via using object area fraction that is less sensitive to swath coverage situations. However, we could expect that this method is still affected by lots of factors such as object feature, observation feature. Under extreme situations, i.e., absolute discontinuity of object points and the very low coverage of object by satellite swath, it is theoretically impossible to derive accurate estimation of the object because of excessive lost of information. In these special cases, available information is deficient and in turn no strategy can be relied on. So other accessorial and experiential schemes should be introduced to perform reasonable scale estimation. In a word, rigorously unbiased estimation is hard to achieve by using swath measurements that is commonly affected by swath-truncation, because the involved information deficiency gives an essential restriction. Such a limitation is rather significant for traditionally used equivalent-area radius method relying on pixel-counting. This study provides a novel concept, using the additional information about object area fraction to deduce the horizontal scale of an arbitrary object. It maybe regarded as a supplement to traditional method.

Acknowledgements: TRMM PR datasets are provided by TRMM Science Data and Information System.

REFERENCES

Arkin P A. 1979. The relationship between fractional coverage of high cloud and rainfall accumulations during GATE over hte B-scale array. *Monthly Weather Review*, **107**: 1382—1387

Arkin P A and Meisner B N. 1987. The relationship between large-scale convective rainfall and cold cloud over the Western Hemisphere during 1982—1984. *Monthly Weather Review*, **115**: 51—74

Del Genio A D and Kovari W. 2002. Climatic properties of tropical precipitating convection under varying environmental conditions. *Journal of Climate*, **15**: 2597—2615

Fraser R H, Li Z and Cihlar J. 2000. Hotspot and NDVI differencing synergy (HANDS): a new technique for burned area mapping over boreal forest. *Remote Sensing of Environment*, **74**: 362—376

Fu Y F and Liu G S. 2003. Precipitation characteristics in mid-latitude east Asia as observed by TRMM PR and TMI. *Journal of Meteorological Society of Japan*, **81**(6): 1353—1369

Fu Y F, Feng J Y, Zhu H F, Li R and Liu D. 2006. Precipitation structures of thermal convective system happened in the central western subtropical pacific anticyclone. *ACTA Meteorologica Sinica*, **20**(2): 232—243

King M D. 1987. Determination of the scaled optical thickness of clouds from reflected solar radiation measurements. *Journal of Atmospheric Sciences*, **44**: 1743—1751

Liu D, Wang Z E, Liu Z Y, Winker D and Trepte C. 2008. A height resolved global view of dust aerosols from the first year CALIPSO lidar measurements. *Journal of Geophysical Research*, **113**, D16214, doi:10.1029/2007JD009776

Machado L A T, Desbois M and Duvel J P. 1992. Structural characteristics of deep convective systems over tropical Africa and the Atlantic ocean. *Monthly Weather Review*, **120**: 392—405

Masunaga H, L'Ecuyer T S and Kummerow C D. 2005. Variability in the characteristics of precipitation systems in the tropical Pacific. Part 1: Spatial structure. *Journal of Climate*, **18**(6): 823—840

McCollum J R and Ferraro R R. 2003. Next generation of NOAA/NESDIS TMI, SSM/I, and AMSR-E microwave land rainfall algorithms. *Journal of Geophysical Research*, 108(D8), 8382, doi:10.1029/2001JD001512

Mohr K I and Zipser E J. 1996. Mesoscale convective systems defined by their 85GHz ice scattering signature: Size and intensity comparison over tropical oceans and continents. *Monthly Weather Review*, **124**: 2417—2437

Nesbitt S W, Zipser E J and Cecil D J. 2000. A census of precipitation features in the tropics using TRMM: Radar, ice scattering, and lightning observations. *Journal of Climate*, **13**(23): 4087—4106

Nesbitt S W and Zipser E J. 2004. An examination of version-5 rainfall estimates from the TRMM microwave imager, precipitation radar, and rain gauges on global, regional, and storm scales. *Journal of Applied Meteorology*, **43**: 1016—1036

Olson W S, Kummerow C D, Heymsfield G M and Giglio L. 1996. A method for combined passive-active microwave retrievals of cloud and precipitation profiles. *Journal of Applied Meteorology*, **35**(10): 1763—1789

Rosenfeld D and Gagin A. 1989. Factors governing the total rainfall yield from continental convective clouds. *Journal of Applied Meteorology*, **28**: 1015—1030

Rossow W B. 1989. Measuring cloud properties from space: A review. *Journal of Climate*, **2**: 201—213

Shige S, Sasaki H, Okamoto K and Iguch T. 2006. Validation of rainfall estimates from the TRMM precipitation radar and microwave imager using a radiative transfer model: 1. Comparison of the version-5 and -6 products. *Geophysical Research Letters*, **33**, L13803, doi:10.1029/2006GL026350

Smith D F, Gasiewski A J, Jackson D L and Wick G A. 2005. Spatial scales of tropical precipitation inferred from TRMM microwave imager data. *IEEE Transactions on Geoscience and Remote Sensing*, **43**(7): 1542—1551

Spinhirne J D, Palm S P, Hart W D, Hlavka D L and Welton E J. 2005. Cloud and aerosol measurements from GLAS: Overview and initial results. *Geophysical Research Letters*, **32**, L22S03, doi:10.1029/2005GL023507

Wang G and Liu L 2007. A multiscale identifying algorithm for heavy rainfall and application in nowcasting, *Chinese Journal of Atmospheric Sciences*, **31**(3): 400—409

利用卫星轨道资料获取降水云团尺度的新方案

刘　奇, 傅云飞, 王　雨

中国科学技术大学　地球和空间科学学院, 大气探测与气候环境实验室 安徽 合肥　230026

摘　要: 提出一种新的统计方案, 以目标面积比为核心度量指标, 并参照连续圆形目标定义目标面积比意义上的等效半径, 实现对目标宏观尺度大小的量化估计。此方法能有效减轻轨道截断效应所造成的目标尺度低估, 可对通过计数类方法得到的目标空间尺度做出有效修正。

关键词: 降水云团, 空间尺度, 目标面积比, 等效半径

中图分类号: TP79　　文献标识码: A

引用格式: 刘　奇, 傅云飞, 王　雨. 2010. 利用卫星轨道资料获取降水云团尺度的新方案. 遥感学报, **14**(4): 774—788
Liu Q, Fu Y F and Wang Y. 2010. Novel algorithm for retrieving spatial scale of precipitating clouds from low-orbiting satellite observations. *Journal of Remote Sensing*. **14**(4): 774—788

1　引　言

由于同天气背景密切相关, 云生消过程中所伴随的云团空间尺度变化对未来天气演变有很好的指示作用, 常作为辅助指标用于临近天气预报(王改利&刘黎平, 2007)。而且与云生命史、云水路径、云光学厚度、云滴有效半径等宏观、微观云物理属性一样, 云团空间尺度在云型判别甚至地表降水量估计中也是重要的参考因子(Rosenfeld & Gagin, 1989)。

地球静止卫星能实现大尺度连续观测, 是获取云和降水宏观结构最主要的手段(Arkin, 1979; Arkin & Meisner, 1987, King, 1987)。基于高分辨率的实时可见光/红外卫星云图, 对特定类型云团的水平尺度分布已经可以给予准确描述(Machado 等, 1992; Rossow, 1989)。但是在降水云团探测方面, 静止卫星可见光/红外手段存在极大困难。云滴的强散射和吸收消光, 该波段的电磁辐射无法穿透较厚的云层, 导致星载辐射计所接收到的大气顶可见光/红外信号中并不包含云下降水强度信息(Olson 等, 1996)。由于可见光/红外观测难以识别瞬时降水云团, 从而也就无法利用此类观测对降水云相关参数做出估计(Smith 等, 2005)。对于降水相关大气参数的遥感测量, 目前仅能依靠具有强穿透能力的微波辐射信号。由于传感器水平分辨率(直接决定于仪器探测波长和卫星轨道高度)的关系, 现有的微波类传感器(包括被动式微波辐射计和主动式降水雷达)只能搭载于轨道高度较低(300—800km)的低轨卫星平台上。例如 Mohr 等分别基于 SSM/I(搭载于美国防卫气象卫星 DMSP)和 TMI(搭载于热带测雨卫星 TRMM)观测的全球尺度统计结果显示, 绝大多数降水云的水平尺度在 100km 以内(Del Genio & Kovari, 2002; Mohr & Zipser, 1996; Nesbitt 等, 2000)。

由于云在空间分布形式上的离散性和其结构本身的不规则性, 在卫星遥感中一般采用基于连续像元计数的方法实现云团尺度估计, 并多以等面积圆半径的形式表征目标对象的水平特征尺度。该处理方法对于静止卫星准全球面图像有很好的效果, 但对于低轨卫星扫描类传感器, 由于横向扫描幅宽十分有限(TRMM 卫星上 TMI 约 760km, PR 仅约 220km), 仅少量云团能被一条探测轨道所完全覆盖。由于多数云团处于轨道边缘(图 1), 造成卫星探测实际上仅获得并计数其部分像元, 因而对目标水平尺度有所低估。

Nesbitt 等 (2000) 的研究结果指出, PR 有限轨道宽度所导致的轨道截断效应, 其影响到的降水系统占到热带地区降水总数约 17%, 而对于中尺度对流系统此比例则高达 82%。因而, 对于具有较大水平尺度(特征水平尺度超过仪器扫描宽度)的系统,

收稿日期: 2009-07-03; 修订日期: 2010-03-22
基金项目: 国家自然科学基金青年项目(编号: 40805007), 中国博士后科学基金(编号: 20080430099、编号: 200801232)。
第一作者简介: 刘奇(1980—), 男, 博士, 2007 毕业于中国科学技术大学, 目前主要从事云和降水卫星遥感研究。E-mail: lqee@ustc.edu.cn。
通讯作者: 傅云飞: E-mail: fyf@ustc.edu.cn。

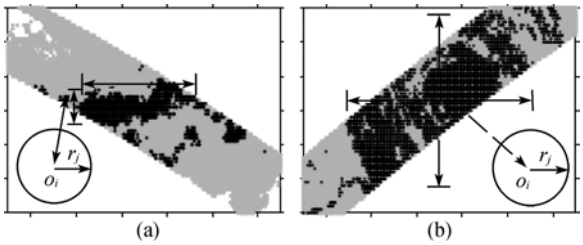

图 1 典型降水云团水平尺度示意

(a) 锋面降水; (b) 台风降水

轨道幅面上黑色像元为降水云, 灰色像元为非降水云, 轨道上其余的少量白色区域为晴空像元。图中 O_i 和 r_j 分别指示后文平均面积比推导中的第 i 个目标参考点和第 j 个参考半径, 其中 O_i 逐一取自作为目标的全体降水云像元

若采取传统云团水平尺度估计方法, 低轨卫星有限轨道观测所导致的面积低估会相当严重。由于在降水面积统计环节存在较高的不确定性, 利用低轨卫星微波资料反演降水强度, 并进而统计获得的地表累积降水量, 其结果的准确性必然受到影响。

另外, 如图 1 所示, 在实际降水云系中, 相对于作为背景的大片连续非降水云区, 降水云结构多样且更趋于散布。基于图像多边形(矩形)的测量方法虽然可以较直观地刻画云团水平尺度(如图 1 中双向箭头所指示的长度和宽度), 但这种方法定量性较差, 对散布其内的非降水云也无法做出有效剔除。而且, 此类基于图像的尺度分析方法仅适用于针对特定系统连续监测的个例分析(傅云飞等, 2005), 无法应用于面向海量卫星资料的程序化处理。基于上述原因, 本文提出一种新的统计方案, 最大程度降低轨道截断效应影响, 利用低轨卫星探测资料对降水云团水平尺度做出更准确的估计。

2 等效半径方案

为表述方便, 并且考虑到方法本身的一般性, 这里的分析不限定于降水云团等具体类别, 而是将待判别水平尺度(或面积)的任何宏观对象称为目标。并且假定在高分辨率像元水平具有对目标点(构成目标的基本单位)的准确识别能力, 即能准确区分目标像元和非目标像元。需要解决的问题是, 如何在已精确获取像元目标于有限轨道上空间分布的前提下, 通过合理的手段减轻轨道截断效应的干扰, 对一定区域范围内的目标宏观水平尺度做出有效度量。该方法与目标所属的具体类别无关, 实际上可适用于所有仅能由低轨卫星实现的高精度目标探测, 如红外/可见光火点监测(Fraser 等, 2000)、微波降水监测(McCollum & Ferraro, 2003; Fu & Liu, 2003; Shige 等, 2006)、激光雷达气溶胶监测等(Spinhirne 等, 2005; Liu 等, 2008)。

像元计数类方法之所以会由于轨道边界截断而对目标面积产生低估, 主要是因为此类方法所统计的目标像元数量是绝对量。该数量主要决定于目标宏观尺度大小, 但同时也与轨道幅面对目标的覆盖程度有关。假设一特定目标仅有一半的面积被探测轨道所覆盖, 则传感器探测到的目标像元数量(相比于实际数量)必然减半, 以此估计的目标面积也相应会有 50%的偏低。而且轨道覆盖比例是一个随机变量, 难以通过确定该参数而达到对上述偏低误差的修正。另一种常用方法——图形图像法的本质其实是在水平面上人为建立正交坐标系, 并以目标像元在两个维度上各自的最大间距作为对目标宏观水平尺度的度量。此方法仅以互为远端的极少数目标像元为有效样本, 忽视了目标内部的散布特性和目标结构的不规则性, 容易对目标面积产生高估。

理想方法的核心即是要找出一种对轨道覆盖比例本身不敏感、或者敏感性较低的相对量, 它能够反映出有限观测区域内所有目标像元相互间的散布程度, 并可作为参考量来进一步确定目标整体的水平尺度。目标像元两两间距离的均值保证了对所有目标像元的等权重采样, 是对该离散程度最直接的一个度量。但是, 容易证明该度量不是相对量, 其数值同样会由于轨道幅面对目标的不完全覆盖而较真值偏低, 因而不是理想的度量参考。

2.1 目标面积比原理

综合以上考虑, 本方法使用核心为目标面积比的统计方案来度量目标的宏观尺度。目标面积比(object area fraction, OAF)可简单理解为, 在指定的参考范围内目标像元数目占观测总像元数目的比例。由于是同等观测, 所有像元的分辨率一致, 所代表的面积也均相等, 因此上述的像元数目比例实际上就是面积比例。对于随机散布且形状各异的有限目标面, 此目标面积比与所指定参考范围的中心位置及大小有关。如果以特定区域内某确定目标像元为中心来指定此参考范围, 由于目标像元在小区域内相对较高的空间连续性, 在参考范围较小时目标面积比接近于 1。随着参考范围的不断增大, 因目标空间尺度的有限性和外围目标像元散布程度的增强, 参考范围内非目标像元的数量会逐渐增长, 目标面积比必然会逐渐减小。

对于给定的参考范围中心, 目标面积比是参考范围大小的单变量函数, 其变化形式对目标像元散布程度有很好的指示意义, 而目标像元散布程度能

一定程度反映目标的大小。采用目标面积比的最大优势在于, 当参考范围达到轨道幅面边缘时, 即由轨道截断所造成的目标伪边界处, 目标面积比这一无量纲相对量会因目标像元和观测像元的同步减少而保持大致定常。由于不会在轨道截断位置出现目标面积比的急速衰减, 从而也就不会给出虚假的目标边界指示。

由于划定参考范围最方便的形式就是圆周, 相应定位参考范围位置可采用参考圆周的圆心。同时为了保证对所用目标像元的等权重采样, 需要对所有目标像元逐一作为参考圆中心, 通过改变参考圆周半径计算其特定的目标面积比随参考半径变化曲线, 最终的目标面积比曲线(平均目标面积比)是对所有目标像元的算术平均。

上述目标面积比的核心思想与 Masunaga 等(2005) 所提出的相关尺度方案基本一致, 但在应用中, 由于实际目标形态的复杂性, 难以准确定位相关尺度方案中所要求的目标面积比急速衰减临界位置。实际情况是, 逐点算术平均获得的平均目标面积比曲线可能并不存在清晰的拐点。本方案中我们类比理想目标, 即连续圆形目标面, 依据下文的数学证明和推导, 建立基于目标面积比的目标等效半径方案。

2.2　理想圆面目标面积比

如前所述, 我们首先定义目标面积比 f, 即在一指定范围内, 目标面积(或目标像元数目)占参考范围总面积(或总像元数目)的比值。为方便计算, 这一参考范围在本方法中设定为圆形。对于有限区域内一个给定位置的目标点(参考点), 以其为圆心再指定参考半径就可完全确定出一参考范围。显然, 因为已假定能够准确区分目标点与非目标点, 落入该参考范围(圆周)内的目标点数量以及目标面积比可以很方便地计算得到。公式(2.2.1)为目标面积比的基本数学定义, 其中 $S(r)$表示半径为 r 的圆周范围内目标点所占的总面积。

$$f(r)=\frac{S(r)}{\pi r^2} \tag{1}$$

这里我们依据理想目标(连续圆形目标面), 计算多种情形下的目标面积比 f。假设连续目标面是半径为 R 的圆面(圆心为 O, 图 2 中灰色圆形区域), 参考点 O' 取自该圆面上(即满足参考点本身是目标点的条件), 且与目标圆心 O 之间的距离为 $l(l\leqslant R)$, 当取参考半径为 r 时, 可计算获得相应的目标面积比 $f(l, r)$。依据参考圆周与目标圆周的位置关系, 目标面积比 $f(l, r)$分如下 3 种情形计算, 如图 2 中(a)、(b)、(c)所示, 以下对这 3 种情形分别进行简要推导。

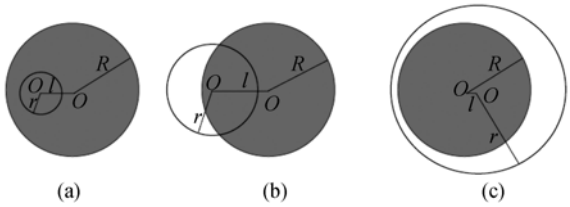

图 2　理想圆形目标 3 种情形下的目标面积比计算原理示意

(1) 参考圆周完全被目标圆周包含, 如图 2(a), 因参考圆内全部为目标点, 所以目标面积比为定值 1, 即有:

$$f_1(l,r)=1,(l\leqslant R, r\leqslant R-l) \tag{2}$$

(2) 参考圆周与目标圆周相交, 如图 2(b), 仅有部分目标点被参考圆周包括, 即参考半径满足条件: $R-l\leqslant r\leqslant R+l$, 令相交的两段圆弧所围区域的面积为 $S(l, r)$, 则有:

$$\begin{aligned}S_2(l,r)=&\,r^2\cos^{-1}\left(\frac{r^2+l^2-R^2}{2rl}\right)+\\&R^2\cos^{-1}\left(\frac{l^2+R^2-r^2}{2lR}\right)-\\&lR\sqrt{1-\left(\frac{l^2+R^2-r^2}{2lR}\right)^2}\end{aligned} \tag{3}$$

目标面积比以如下公式表示:

$$\begin{aligned}f_2(l,r)=&\,S(l,r)/\pi r^2\\=&\,\frac{1}{\pi}\cos^{-1}\left(\frac{r^2+l^2-R^2}{2rl}\right)+\\&\frac{R^2}{\pi r^2}\cos^{-1}\left(\frac{l^2+R^2-r^2}{2lR}\right)-\\&\frac{lR}{\pi r^2}\sqrt{1-\left(\frac{l^2+R^2-r^2}{2lR}\right)^2}\end{aligned} \tag{4}$$

(3) 参考圆周完全包含目标圆周, 如图 2(c), 此时参考半径满足条件: $r\geqslant R+l$。由于目标区域已完全被参考圆周所包围且目标面积为有限定值, 此时目标面积比将随参考圆面积成单调反比变化, 相应的目标面积比表示为:

$$f_3(l,r)=\frac{\pi R^2}{\pi r^2}=\frac{R^2}{r^2} \tag{5}$$

通过以上公式, 对于取自目标圆面上的任一参考点, 计算获得满足相应取值范围条件的目标面积比。需要指出的是, 上述针对不同情形的目标面积比公式受到参考半径范围的限制, 实际当 l 处于特定位置(如 l_0)时, $f(l_0, r)$在 r 的整个有效变化域内为分

段函数,其各段的函数形式将分别为 f_1、f_2 或 f_3。

依据上述相关公式, 图 3 给出了 3 种特殊参考点位置的圆形目标面积比计算结果, 其中三条曲线, 简称为 $f(0)$、$f(R/2)$和 $f(R)$, 分别代表参考点在目标圆的圆心、1/2 半径和圆周上的面积比变化形式。显然, $f(R/2)$的曲线代表了圆面上一般目标点(非圆心和圆周)作为参考点时, 目标面积比随参考半径变化的普遍形式。如图 3, $f(R/2)$在整个参考半径域上是连续曲线, 其分别在 $0.5R$ 和 $1.5R$ 处有两个一阶导数不连续点, 对应位置的目标面积比分别为 1.0 和 0.444。其在参考半径小于 $0.5R$ 时, 目标面积比恒为 1.0, 参考半径超过 $1.5R$ 以后, 目标面积比随参考半径满足简单的二次反比变化。$2R$ 位置是 3 条曲线的交汇点, 当参考半径超过 $2R$ 后, 不管参考点位于圆面上何处, 目标面积比都将随参考半径呈二次方反比变化。

参考点的位置限定为仅可取自任一目标点(图 2 中灰色圆面上任一点), 这是因为只有将目标点作为参考圆心, 当参考半径 r 从 0 开始增大时, 目标面积比会从 1(若参考圆心处于连续目标区域的边缘, 并假设目标像元为理想点且目标边界为连续曲线, 可严格证明该极限值为 0.5)开始逐渐减小(理论上也存在短暂增加的可能, 但实际中其所对应的像元分布形式的出现概率极低, 因而在后面算术平均中的权重贡献可忽略不计)。当 r 逐渐增大时如果 $f(l,r)$ 快速减小, 指示非目标点的增长率已大于目标点的增长率, 表明该相对距离处的目标点已极少出现, 接近目标边缘。而如果将非目标点也作为参考点计算目标面积比, 会造成诸多困难。首先, 用于统计的非目标点的数目难以界定(这里暗含假设, 即目标像元在探测像元总数中为小量, 对于降水云团卫星遥感, 该假设符合实际情况), 而且, 其目标面积比变化趋势中不包含明确的目标水平尺度信息。特别, 仅以目标点逐一作为参考圆心进行目标面积比的计算, 可以对小尺度独立目标(零星孤立降水系统)达到快速甄别和尺度估计。

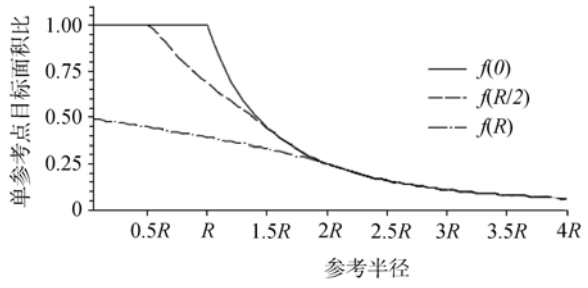

图 3 连续圆形理想目标的特殊参考点目标面积比计算结果

实线、虚线和点划线分别为参考点取自圆心、1/2 半径和圆周上的目标面积比

2.3 标准平均目标面积比曲线

由以上公式计算出的目标面积比 $f(l, r)$除与参考半径 r 有关外, 还是参考圆心位置(与 l 有关)的函数。如前所述, 我们期望得到的是可反映宏观目标整体尺度特征的目标面积比随 r 的变化关系。因此, 最终可代表一定区域范围的目标面积比统计结果, 理论上来自于给定参考半径 r_j (角标 j 指示实际计算中的离散采样, 图 1)条件下, 对全部(假设为 n 个)参考点 O_i 的目标面积比的算术平均。为区分于前述的单参考点目标面积比, 该逐点平均的结果我们称之为平均目标面积比, 以 F 表示, 即有如下关系:

$$F(r_j)=\frac{1}{n}\sum_{i=1}^{n} f(O_i,r_j) \tag{6}$$

对于理想圆形目标, 上式等价于圆面上的积分, 即:

$$\begin{aligned} F(r)&=\frac{1}{S}\int_{S_R} f(l,r)\mathrm{d}S \\ &=\frac{1}{\pi R^2}\int_0^R f(l,r)\times 2\pi l\mathrm{d}l \end{aligned} \tag{7}$$

显然, 给定 r, 当 l 由 0 增至 R 的过程中, $f(l,r)$ 的函数形式不定(f_1, f_2, f_3), 需要进行分段积分, 而且该分段的确定与 r 有关。简单起见, 我们可以将 r 的变化域分为 3 部分, 分别进行分段积分计算。

(1) 当 $r\leqslant R$ 时, 有:

$$\begin{aligned} F(r)&=\frac{1}{\pi R^2}\left[\int_0^{R-r} f_1(l,r)\times 2\pi l\mathrm{d}l+\int_{R-r}^{R} f_2(l,r)\times 2\pi l\mathrm{d}l\right] \\ &=\frac{(R-r)^2}{R^2}+\frac{2}{R^2}\int_{R-r}^{R} f_2(l,r)\times l\mathrm{d}l \end{aligned} \tag{8}$$

(2)当 $R<r\leqslant 2R$ 时, 有:

$$\begin{aligned} F(r)&=\frac{1}{\pi R^2}\left[\int_0^{r-R} f_3(l,r)\times 2\pi l\mathrm{d}l+\int_{r-R}^{R} f_2(l,r)\times 2\pi l\mathrm{d}l\right] \\ &=\frac{(r-R)^2}{r^2}+\frac{2}{R^2}\int_{r-R}^{R} f_2(l,r)\times l\mathrm{d}l \end{aligned} \tag{9}$$

(3)当 $r>2R$ 时, 有:

$$F(r)=\frac{1}{\pi R^2}\int_0^R f_3(l,r)\times 2\pi l\mathrm{d}l=\frac{R^2}{r^2} \tag{10}$$

由于 $f_2(l, r)$的复杂函数形式, 上述积分无法在 $r\leqslant 2R$ 范围获得解析解, 只能以数值积分形式获得数值近似结果, 图 4 给出了连续圆面的平均目标面积比数值积分结果, 即理想目标的标准平均面积比曲线。如图 4 所示, 平均目标面积比仅在参考半径逼近 0 时接近于 1.0, 此后随参考半径增大呈现为快

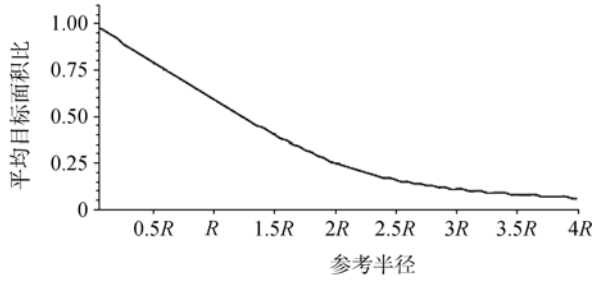

图 4　连续圆面理想目标平均目标面积比数值积分结果

速递减趋势，在经过定点(*2R*, 0.25)后，递减趋势渐缓。此结果显示，不同于给定参考点的目标面积比，平均目标面积比在参考半径处于 0—*2R* 范围一直保持大幅衰减。如果注意曲线的斜率变化情况，可以发现参考半径从 0—*4R* 的变化过程中，平均目标面积比的变化率一直在减小，并未有明显突变，即不存在可用作确定 Masunaga 等 (2005) 方案中相关尺度的特殊参考半径位置。因此，利用整条平均面积比曲线信息来获得对实际目标尺度的估计是更为合理的方式。

2.4　目标面积比等效半径导出

综合上述分析，本方案拟利用基于最小方差的相似曲线法，完成对实际平均目标面积比曲线和理想圆标准曲线的比对，以获得预期的目标面积比等效半径(Equivalent-OAF Radius)。

对实际离散像元，通过合适的计算方案可获得 $F(d_i),(i=1,M)$，其中 d_i 是算法中对参考半径(具有长度单位的具体物理量)的离散设定，参考半径总数为 M。需要实现的是，通过对 $F(d_i)$进行固定 0 点(左端点)的伸缩变换，以达到与理想圆数值结果曲线 $F(r)$ 的最大相似度。如当 $j=K$ 时，满足曲线段 $F(d_j),(j=1, K)$和曲线段 $F(r),(r=0, 4R)$最相似，即各对应位置 F 值的累积方差最小。这时的 d_K 就对应 *4R*，相应 $d_k/4$ 就定义为目标面积比等效半径。

注意到本方案中我们选择的理想圆参照曲线段是 *0—4R* 段。这是因为以 *2R* 为界，理想圆面平均目标面积比 $F(r)$ 的函数形式在前后两段完全不同，因而该段曲线包含了最充分的曲线特征。由于在计算不同伸缩变换下的方差时，需要在两曲线上进行等量采样，实际计算方案中，一般将 d_i 设定为等间距变化，即Δd 为定值。因此我们对 $F(r),(r=0, 4R)$也进行均分采样，假设采样点数量为 K，则对于理想曲线等价于已知:

$$\begin{cases} F(r_i), i=1,K \\ r_i = i\times\Delta r = \dfrac{i\times 4R}{K} \end{cases} \tag{11}$$

对实际曲线则需进行逐次伸缩变换，以获得等间距的 K 个采样点。基本变换(伸缩比 q=1)即是取原始序列中最左边的 K 个样点 $d_i(i=1,K)$。为保证计算都来自原始采样位置，避免相邻若干个采样点值的平均，伸缩比 q 均取为正整数(1, 2, 3…,)，显然 q 有上限 $\mathrm{int}(\dfrac{M}{K})$，相应对于实际曲线等价于已知:

$$\begin{cases} F(d_i), i=q,qK,q \\ d_i = i\times q\times\Delta d \end{cases} \tag{12}$$

实际问题转化为求 q_0，如果令目标函数是样本量为 K 的两序列间方差 $D(\Delta d,q,K)$，则所求的 q_0 需满足下列条件:

$$D(\Delta d,q,K)\big|_{q=q_0} \to \min\left\{D(\Delta d,q,K)\right\} \tag{13}$$

一旦获得 q_0，则有目标面积比等效半径:

$$R_0 = \frac{d_{Kq_0}}{4} = \frac{Kq_0\times\Delta d}{4} \tag{14}$$

上面数学推导过程的本质可以简单描述为，在由 M 个点(位置由 x 和 y 轴坐标唯一决定，x 轴间距为定值Δd)组成的原始曲线上，逐一挑出 $K(K<<M)$ 个点(x 轴间距为定值$\Delta d'$)组成新的曲线，满足$\Delta d'$是Δd 的整数倍，如果在某一$\Delta d'$下，新曲线达到与理想圆参考曲线最大相似，该曲线右端点 x 坐标即是 *4R*。

因为 q 的取值存在上限 $\mathrm{int}\left(\dfrac{M}{K}\right)$，所以有:

$$R_0 = \frac{Kq_0\times\Delta d}{4} \leqslant \frac{M\times\Delta d}{4} = \frac{L}{4} \tag{15}$$

其中 L 可认为是统计区域的最大尺度。上式表明 L 的取值要足够大，否则会因原始采样信息的不足，使得曲线搜索过程仅能获得有条件的最大相似，而非绝对最大相似曲线，相应的等效半径结果会存在系统偏差。另外，由于 q 仅可取正整数，即有 q_0 解的精度Δq 为 1，R_0 的精度可表示为:

$$\Delta R = \frac{K\times\Delta q\times\Delta d}{4} = \frac{K\times\Delta d}{4} \tag{16}$$

由上式可知，R_0 的精度除了Δd 有关外，还与 K 有关，因此 K 的取值不可过大，但同时为保证在两曲线上的充分采样以便准确计算曲线相似度，K 值也不能过小。对于本方法所针对的实际 TRMM PR 轨道观测，Δd 取为 5km(接近 PR 像元水平分辨率)，K 取值为 20，相应 R_0 的计算精度为 25km。

3　实例应用

利用 TRMM PR 轨道降水资料(TRMM 卫星 2001 年 8 月升轨后 PR 像元水平分辨率约 4.9km，横

向扫描幅宽约 250km, Nesbitt & Zipser, 2004), 对目标面积比等效半径方案进行了实例应用, 选取的样本为 2005 年夏季东亚陆地及附近洋面上的锋面和台风降水个例。基于前面的分析, 考虑到锋面降水云团和台风降水云团的显著形态差异, 预先将个例归类, 然后对两类样本(锋面降水 12 例, 台风降水 11 例)中的个例逐一进行等效半径计算, 最后依据统计平均对两类降水云团特征尺度做出估计。

实际计算中的遍历区域取为经度方向 10°的轨道片断(满足前面分析中 L 足够大的要求), 遍历总像元数目不超过 16000, 参考半径采样间距Δd 为 5km, 最大采样距离取至 2000km。图 5(a)和图 5(c)给出了两类样本逐一的目标面积比计算结果。实际目标面积比曲线相比理想圆目标面积比曲线有不同程度的偏离, 其中锋面降水云团平均目标面积比曲线相互间差异更大, 多个台风降水云团具有相近的平均目标面积比变化形式。这一结果与台风降水云团多为近圆形或近圆环型的基本结构有关, 同时也表明尽管锋面降水多呈东西向带状发展, 但在云团水平尺度和形态上均存在较大的变化。

图 5(b)和图 5(d)为最小方差目标面积比曲线, 相比于理想圆目标的参考曲线, 实际样本的最小方差曲线都更趋于平缓, 即在参考半径较小时数值偏低, 在参考半径较大时偏高。这种结果与实际目标非完全连续有关, 特别是在目标外围一般不存在简单划一的边界。如图 5(b), 锋面降水中有 2 例尽管已是最小方差曲线, 但仍偏离标准曲线较远, 这与该例降水的强散布性有关, 导致完全不能近似于连续圆面。依据最小方差曲线, 最终可得到等效半径结果对于锋面降水和台风降水分别为 283±163km 和 297±126km。结果表明, 锋面与台风系统中降水云团的水平尺度差异不显著, 后者仅高出前者约 5%。同时, 锋面样本较大的标准差(超过其均值的 50%)显示其水平尺度个体差异更大。

此外, 以像元计数法分别计算了上述降水云团样本的等面积半径, 结果为锋面样本 172±52km, 台风样本 181±25km, 对应两种方案的逐一对比结果如图 6(a)和图 6(b), 对于等面积半径大于 150km 的绝大多数降水云团, 本方案给出的等效半径均明显大于等面积半径, 最高可达后者的 2 倍。考虑到约 250km 的 PR 幅宽, 这一结果显示, 统计获得的等面积直径一旦超过传感器横向扫描幅宽, 该结果很可能已受到轨道截断效应的影响(图 1(b)), 即数值有所偏小。而且等面积半径越大, 计数法漏掉的目标像元越多, 偏小程度越大, 反映在图 6 上即散点偏离对角线越远。目标面积比等效半径受轨道截断效

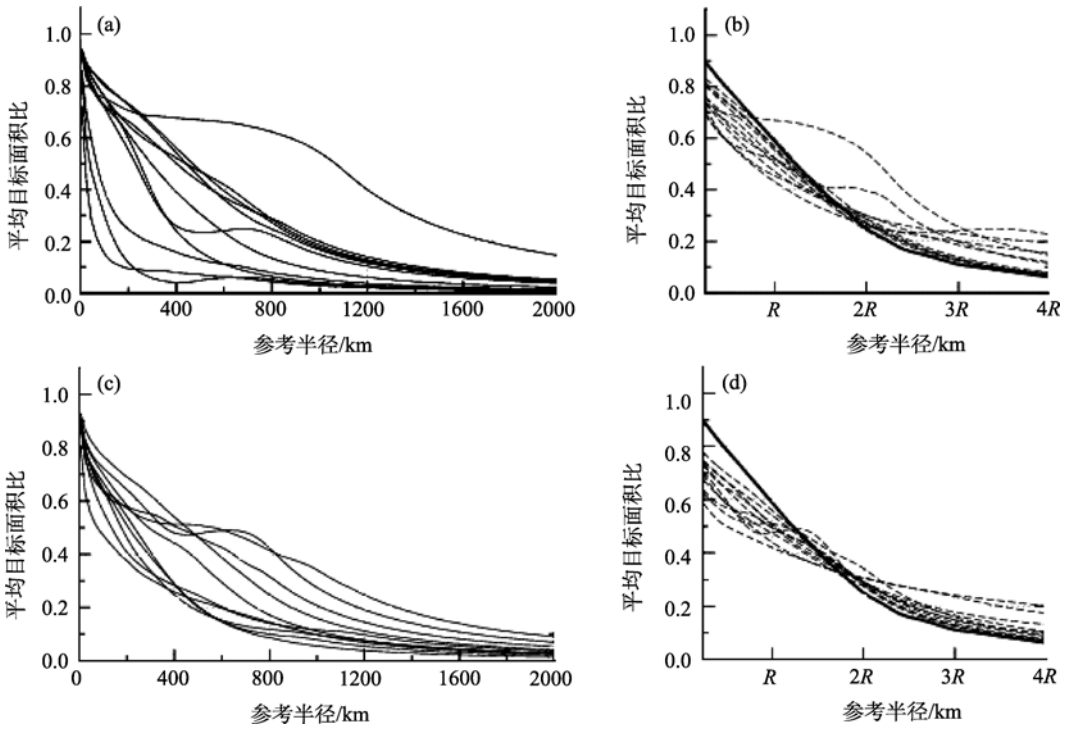

图 5 实例样本目标面积比计算结果

左列为锋面(a)和台风(c)样本的平均目标面积比,(b)和(d)中虚线分别为相应个例用于求解目标面积比等效半径的最小方差曲线, 实线为理想圆目标面积比标准曲线

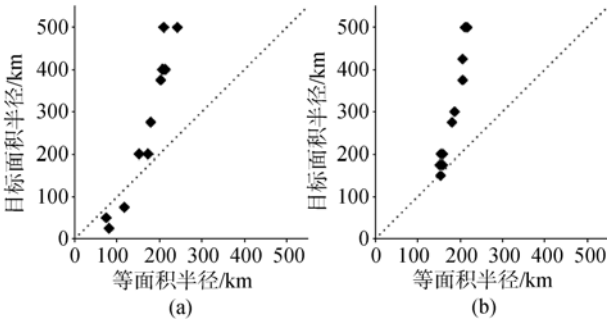

图 6　像元计数等面积半径和目标面积比等效半径差异统计, (a)锋面样本和(b)台风样本

应影响较小，其较等面积半径能更准确地描述目标水平尺度。另外，如果不关注两种计算方案的数值差异，目标面积比等效半径和等面积半径结果一致反映了台风降水云团的尺度相似性。

4　讨　论

由于真实目标形态结构的非规则性，参照圆形目标并以等面积半径描述其水平尺度是最常用的手段。然而在低轨卫星应用中，该面积等效方案往往因轨道截断现象的存在而导致结果偏低。本研究提出了一种新的方法，以圆形目标的目标面积比为等效参考量，利用它对轨道截断效应的低敏感性，获得在目标面积比(相对于传统方案的面积)上具有最大相似度的等效半径，来指示更为准确的目标水平尺度。实际上和面积这一标量参考量一样，目标面积比(随参考半径变化形式)可看作一矢量，它同样是对特定目标大小的一个描述。计算所得的真实目标面积比一旦和圆目标达到极大相似，那么在目标面积比意义上，该圆半径就可同样作为等效半径来指示真实目标尺度大小。

需要指出的是，依据本方案获得的目标面积比等效半径同样不是目标空间尺度的一个直接度量，因而不能简单以该等效半径估算目标的真实面积。由于实际轨道截断情况的复杂性，将目标面积比等效半径与目标真实面积联系起来，以获得此结果更明确的指示意义，还必须借助于足够多实验样本下的统计分析。考虑到像元计数这类基于面积的方法(尽管存在低估)本质上与目标面积有更为直接的联系，因此一个在实际应用中的理想简化方案是两类方法的结合使用，即以像元计数法获得对目标尺度的初步估计，结合目标面积比等效半径方案对前一步可能的偏低结果给予修正。

对于目标面积比等效半径方案，本文目前仅提出了完整的数学方案，但对该等效半径方案所暗含的对轨道截断效应的抑制作用，还未进行有针对性的量化评估。这是因为该作用与实际观测有关，目标本身的形态结构和其在轨道上的分布情况会对本方案的结果产生重要影响。有统计意义的方案评估将来自于对大量仿真实例(真实目标面积已知，计算机数值模拟有限幅宽轨道对随机形态目标的随机覆盖)的模拟研究，这些工作正在进行之中。同时需要特别指出，利用目标面积比对轨道截断的低敏感性，等效半径方案理论上可实现对轨道截断效应的减缓。但可以预计的是本方案的有效性仍受到诸如目标特性、观测特性等多种因素的影响，如目标连续性极差、轨道覆盖率过低等。这种极端情形下，因为可获取信息本身的过度丢失，本质上已无法实现对目标尺度的更准确估计。此情况下，除了本文提出的基于目标面积比的统计方案外，其他辅助策略和充分的先验信息将会为降低结果误差起到积极作用。因此，尽管难以对目标尺度获得严格意义上的无偏估计，但本文所提出的方案提供了一种新思路，可作为补充对传统计数类方法的偏低结果给予有效修正。

致　谢: 热带测雨卫星(TRMM)测雨雷达(PR)和可见光红外扫描仪(VIRS)资料由TRMM科学数据信息系统(TSDIS)提供，特此感谢。

REFERENCES

Arkin P A. 1979. The relationship between fractional coverage of high cloud and rainfall accumulations during GATE over hte B-scale array. *Monthly Weather Review*, **107**: 1382—1387

Arkin P A and Meisner B N. 1987. The relationship between large-scale convective rainfall and cold cloud over the Western Hemisphere during 1982—1984. *Monthly Weather Review*, **115**: 51—74

Del Genio A D and Kovari W. 2002. Climatic properties of tropical precipitating convection under varying environmental conditions. *Journal of Climate*, **15**: 2597—2615

Fraser R H, Li Z and Cihlar J. 2000. Hotspot and NDVI differencing synergy (HANDS): a new technique for burned area mapping over boreal forest. *Remote Sensing of Environment*, **74**: 362—376

Fu Y F and Liu G S. 2003. Precipitation characteristics in mid-latitude east Asia as observed by TRMM PR and TMI.

Journal of Meteorological Society of Japan, **81**(6): 1353—1369

Fu Y F, Feng J Y, Zhu H F, Li R and Liu D. 2006. Precipitation structures of thermal convective system happened in the central western subtropical pacific anticyclone. *ACTA Meteorologica Sinica*, **20**(2): 232—243

King M D. 1987. Determination of the scaled optical thickness of clouds from reflected solar radiation measurements. *Journal of Atmospheric Sciences*, **44**: 1743—1751

Liu D, Wang Z E, Liu Z Y, Winker D and Trepte C. 2008. A height resolved global view of dust aerosols from the first year CALIPSO lidar measurements. *Journal of Geophysical Research*, **113**, D16214, doi:10.1029/2007JD009776

Machado L A T, Desbois M and Duvel J P. 1992. Structural characteristics of deep convective systems over tropical Africa and the Atlantic ocean. *Monthly Weather Review*, **120**: 392—405

Masunaga H, L'Ecuyer T S and Kummerow C D. 2005. Variability in the characteristics of precipitation systems in the tropical Pacific. Part 1: Spatial structure. *Journal of Climate*, **18**(6): 823—840

McCollum J R and Ferraro R R. 2003. Next generation of NOAA/NESDIS TMI, SSM/I, and AMSR-E microwave land rainfall algorithms. *Journal of Geophysical Research*, 108(D8), 8382, doi:10.1029/2001JD001512

Mohr K I and Zipser E J. 1996. Mesoscale convective systems defined by their 85GHz ice scattering signature: Size and intensity comparison over tropical oceans and continents. *Monthly Weather Review*, **124**: 2417—2437

Nesbitt S W, Zipser E J and Cecil D J. 2000. A census of precipitation features in the tropics using TRMM: Radar, ice scattering, and lightning observations. *Journal of Climate*, **13**(23): 4087—4106

Nesbitt S W and Zipser E J. 2004. An examination of version-5 rainfall estimates from the TRMM microwave imager, precipitation radar, and rain gauges on global, regional, and storm scales. *Journal of Applied Meteorology*, **43**: 1016—1036

Olson W S, Kummerow C D, Heymsfield G M and Giglio L. 1996. A method for combined passive-active microwave retrievals of cloud and precipitation profiles. *Journal of Applied Meteorology*, **35**(10): 1763—1789

Rosenfeld D and Gagin A. 1989. Factors governing the total rainfall yield from continental convective clouds. *Journal of Applied Meteorology*, **28**: 1015—1030

Rossow W B. 1989. Measuring cloud properties from space: A review. *Journal of Climate*, **2**: 201—213

Shige S, Sasaki H, Okamoto K and Iguch T. 2006. Validation of rainfall estimates from the TRMM precipitation radar and microwave imager using a radiative transfer model: 1. Comparison of the version-5 and -6 products. *Geophysical Research Letters*, **33**, L13803, doi:10.1029/2006GL026350

Smith D F, Gasiewski A J, Jackson D L and Wick G A. 2005. Spatial scales of tropical precipitation inferred from TRMM microwave imager data. *IEEE Transactions on Geoscience and Remote Sensing*, **43**(7): 1542—1551

Spinhirne J D, Palm S P, Hart W D, Hlavka D L and Welton E J. 2005. Cloud and aerosol measurements from GLAS: Overview and initial results. *Geophysical Research Letters*, **32**, L22S03, doi:10.1029/2005GL023507

Wang G L and Liu L P. 2007. A multiscale identifying algorithm for heavy rainfall and application in nowcasting, *Chinese Journal of Atmospheric Sciences*, **31**(3): 400—409

附中文参考文献

傅云飞, 冯静夷, 朱红芳, 李锐, 刘栋. 2005. 西太平洋副热带高压下热对流降水结构特征的个例分析. 气象学报, **63**(5): 750—761

王改利, 刘黎平. 2007. 暴雨云团的多尺度识别方法及其在临近预报中的应用. 大气科学, **31**(3): 400—409